nature communications

Article

https://doi.org/10.1038/s41467-024-51466-8

Energy-efficient $CO_{(2)}$ conversion to multicarbon products at high rates on CuGa bimetallic catalyst

Received: 27 January 2024

Accepted: 8 August 2024

Published online: 15 August 2024

Check for updates

Lei Chen[1], Junmei Chen[1], Weiwei Fu[1], Jiayi Chen[1], Di Wang[1], Yukun Xiao[2], Shibo Xi[3], Yongfei Ji[4] ✉ & Lei Wang[1,5] ✉

Electrocatalytic CO_2 reduction to multi-carbon products is a promising approach for achieving carbon-neutral economies. However, the energy efficiency of these processes remains low, particularly at high current densities. Herein, we demonstrate that the low energy efficiencies are, in part, sometimes significantly, attributed to the high concentration overpotential resulting from the instability (i.e., flooding) of catalyst-layer during electrolysis. To tackle this challenge, we develop copper/gallium bimetallic catalysts with reduced activation energies for the formation of multi-carbon products. Consequently, the reduced activation overpotential allows us to achieve practical-relevant current densities for CO_2 reduction at low cathodic potentials, ensuring good stability of the catalyst-layer and thereby minimizing the undesired concentration overpotential. The optimized bimetallic catalyst achieves over 50% cathodic energy efficiency for multi-carbon production at a high current density of over 1.0 A cm^{-2}. Furthermore, we achieve current densities exceeding 2.0 A cm^{-2} in a zero-gap membrane-electrode-assembly reactor, with a full-cell energy efficiency surpassing 30%.

Electrochemical reduction of carbon dioxide/monoxide (CO_2/COR) to valuable fuels and chemicals, powered by renewable electrical energy, emerges as a promising approach for achieving carbon neutrality and advancing sustainability transition[1–3]. Currently, achieving practical relevant CO_2R/COR current density (>0.2 A cm^{-2}) and selectivity (in regard of Faradaic Efficiency, FE > 80%) for the production of multi-carbon (C_{2+}) products e.g., ethylene (C_2H_4)[4,5], ethanol (C_2H_5OH)[6,7], acetate[8,9], and *n*-propanol[10,11], are feasible by employing Cu-based catalysts. However, a noteworthy challenge that often gets overlooked is achieving sufficiently high energy efficiency (EE), especially at high current densities (>1 A cm^{-2})[12,13]. To enhance energy efficiency, it's essential to understand and be able to tune the components of overpotential during catalysis. Generally, the overall cathodic overpotentials (η_{tot}) primarily consist of three distinct elements: activation (η_{act}), concentration ($\eta_{con.}$), and ohmic overpotentials (η_{ohmic})[14]. Taking C_2H_4 production as an example (Fig. 1a), the total overpotential for C_2H_4 production can be described by Eq. (1):

$$\eta_{tot} = \eta_{act.} + \eta_{con.} + \eta_{ohmic} \quad (1)$$

Tremendous efforts have been devoted to minimizing these three overpotentials[15,16]. Various catalyst development strategies, such as tuning oxidation state[17,18], alloying[19,20], and non-metal element doping[21], have been developed for achieving improved activity, resulting in reduced activation overpotential. Besides, tuning microenvironment at the reaction interface has been demonstrated to effectively alter both the activation overpotential and concentration

[1]Department of Chemical and Biomolecular Engineering, National University of Singapore, Singapore, Singapore. [2]Department of Chemistry, National University of Singapore, Singapore, Singapore. [3]Institute of Sustainability for Chemicals, Energy and Environment, A*STAR, Singapore, Singapore. [4]School of Chemistry and Chemical Engineering, Guangzhou University, Guangzhou, Guangdong, China. [5]Centre for Hydrogen Innovations, National University of Singapore, E8, Singapore, Singapore. ✉e-mail: yongfeiji2018@gzhu.edu.cn; wanglei8@nus.edu.sg

https://doi.org/10.1038/s41467-024-51466-8

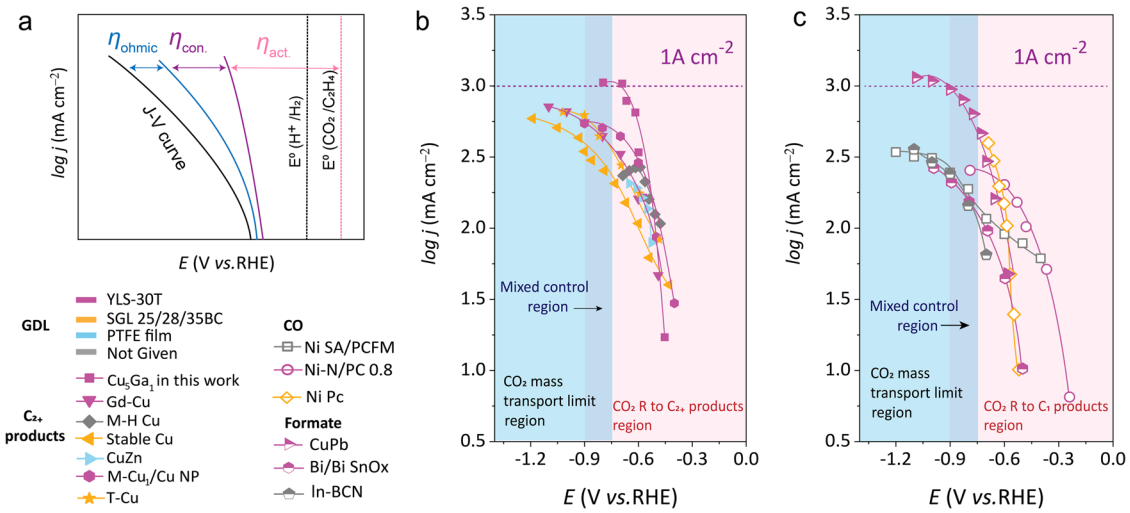

Fig. 1 | Analysis of current-potential correlations for CO_2R. a illustrations of activation, concentration, and ohimc overpotentials for C_2H_4 production. **b**, **c** The partial current density of C_{2+}, CO, and HCOOH as function of applied potentials. The different colors represented different commercial GDL types. The data were adopted form these literatures: Gd-Cu[20], M-H Cu[27], Stable Cu[23], CuZn[13], M-Cu$_1$/Cu NP[28], T-Cu[29], NiSA/PCFM[32], Ni-N/PC0.8[33], NiPc[34], CuPb[35], Bi/Bi SnOx[36],In-NCN[37]. Relevant source data are provided in the Source Data file.

overpotential[22,23]. Furthermore, there has been extensive recent exploration of the zero-gap membrane electrode assembly (MEA), formed by directly pressing the cathode gas diffusion electrode (GDE) and anode catalyst on each side of the ion exchange membrane, aiming to minimize the ohmic overpotentials across the reactor[24–26]. Despite significant progress achieved through the above strategies, the energy efficiency of CO_2R/COR remains in its infancy, particularly at high current densities (EE below ~10–20% at >1 A cm^{-2})[4,12].

To tackle on this grand challenge, we carefully examined the correlations between the apparent current density and the applied cathodic potential using data obtained from the recently developed state-of-the-art Cu-based catalysts (Supplementary Table 1)[13,20,23,27–29]. Surprisingly, even though from different studies, we observed similar potential dependent-current density trends when plotting these data together, as shown in Fig. 1b. Inspired by previous research[30,31], we assumed that this trend can be divided into three distinct areas for analysis: a common primary activation-controlled kinetic region within the potential range of approximately −0.2 to −0.7 V versus the reversible hydrogen electrode (V_{RHE}), followed by a mixed-controlled kinetics region (~−0.75 to −0.9 V_{RHE}), and then a severely mass-transport-controlled kinetic region at high potentials (~−0.9 to −1.2 V_{RHE}) for these documented Cu-based electrocatalysts. We reasoned that the onset of CO_2 mass transfer limitation, starting from the mixed-control potential region, could be attributed to two factors: (1) insufficient intrinsic CO_2 gas transport capability of the commercial GDE materials (such as YLS-30T, SGL-28BC, and PTFE film, etc.,); (2) reaction interface destruction, such as flooding and salt precipitation at the catalyst layer, resulting in substantially increase in concentration overpotential for CO_2R and favouring the competing reaction of hydrogen evolution reaction (HER). To validate the first hypothesis, we conducted a similar analysis on the state-of-the-art CO_2R systems for CO and formate production[32–37]. We observed that CO and/or formate could be formed at even higher current density within this mixed-control region using the same GDE materials (Fig. 1c, Supplementary Tables 2, 3). Considering that each CO_2 molecules requires fewer electrons to form CO and formate compared to other C_{2+} products, we believe the surface concentration of CO_2 on conventional GDE is sufficient to support higher C_{2+} current. Thus, the observed CO_2 mass transport limitations are likely a result of catalyst layer flooding/carbonate salt precipitation, which we believe is, at least partially, associated with the applied cathodic potential. This observation aligns well with recent studies that indicate a correlation between the applied voltage and the H_2O content across the GDE layer[14,31,38,39]. Therefore, if a catalyst candidate can afford a sufficient CO_2R current with a small applied cathodic potential before entering the mixed-control region, we can anticipate significantly enhanced CO_2R stability, concurrently, enhanced EE at high current densities.

To validate the above hypothesis, it is essential to develop electrocatalysts with enhanced intrinsic activity for CO_2R. Previously, bimetallic materials have demonstrated promise in improving the CO_2/COR performance through various mechanisms, including electronic effect[8,40], strain effect[41,42], and geometric effect[8,43,44]. For example, alloying Cu with different oxyphilic Lanthanide metals can regulate the adsorption energies of key intermediates (*CO and *CH_xO) on Cu, thereby enhancing the production of C_2H_4 and CH_4[45]. Therefore, it could be an effective approach for our purpose. Gallium (Ga) exhibits strong oxygen affinity and reduced electronegativity than Cu[46–48]. Besides, previous studies have shown that *CO binds weakly on Ga[49,50], thereby, by incorporating Ga into Cu, we anticipate the ability to tune the CO adsorption behavior on Cu, with the aim of achieving enhanced intrinsic activity. During the preparation of our manuscript, a couple of CuGa bimetallic catalysts were studied elsewhere very recently. Raffaella et al. found that the Ga can stabilizes the valence state of Cu at the open-circuit potential (OCV), and the interaction between Cu and Ga greatly improved the structure stability of nanoparticles under the operating conditions of CO_2R[51]. Meanwhile, Han et al. and Zheng et al. found that Cu-Ga bimetallic catalysts can result improved selectivity towards C_{2+} products, i.e., FE exceeding 70%[52,53]. Nevertheless, these studies primarily focused on exploring the changes of C_{2+} product in CO_2R selectivity after doping Cu with Ga, here we focus on detailed explorations on whether Ga doping could enhance the intrinsic activity of Cu towards $CO_{(2)}R$.

In this work, our objective is to develop a guiding strategy to achieve high EE, i.e., reduce activation overpotential and maintain low concentration overpotential. Specifically, we employed an alloying–dealloying strategy to synthesize Cu-Ga bimetallic catalysts with enhanced activity for CO_2/CO conversion. Using this CuGa bimetallic material as a model catalyst, we demonstrated that low activation overpotential is critical for achieving high current densities while maintaining low concentration overpotential, consequently,

enhancing EE. We found that minor Ga doping onto the Cu surface can lower the activation energy of CO_2 to *COOH and binding energy of *CO on the Cu-Ga site, promoting CO production at reduced overpotentials in the CO_2R. The resulting increased local CO concentration, combined with the defect-rich sites originated from the dealloying process, significantly boost the C-C coupling process, thereby achieving improved C_{2+} current density at low overpotentials. As we anticipated, the low activation overpotential of CuGa allows the GDE to operate within the kinetic-controlled region, minimizing the concentration overpotential induced by catalyst layer flooding. As a result, the CuGa-based GDE in this study achieved high cathodic energy efficiency exceeding 50% for C_{2+} products at high current density of 1 A cm^{-2}. To further reduce the ohmic overpotential, we assessed the CuGa catalyst in a zero-gap MEA reactor. Likewise, enhanced EE were achieved for both CO_2R and COR. Particularly for COR, a high current density of 2.5 A cm^{-2} was achieved at a low cell voltage of ~3 V. At 1 A cm^{-2}, high EE exceeding 35% was obtained for C_{2+} production surpassing literature benchmarks. Furthermore, as anticipated, the CuGa based-GDE exhibited a stable CO_2R and COR performance. It maintained ~90% C_{2+} Faraday efficiency (FE) during continuous COR operation for up to 120 h (at 0.3 A cm^{-2}), whereas the counter sample Cu-GDE only lasted less than 20 h under identical conditions. Overall, our study demonstrates that optimizing the adsorption behavior of reaction intermediates could effectively reduce activation overpotential for $CO_{(2)}R$. This reduced activation overpotential, in turn, helps maintain low concentration overpotential, facilitating the energy-efficient electrosynthesis of C_{2+} products from $CO_{(2)}$.

Results

Synthesis and characterization of Cu and bimetallic CuGa catalysts

The Cu and CuGa catalysts were synthesized via a one-step reduction procedure (see Method). By varying the feed ratio of Cu^{2+} and Ga^{3+}, a series of CuGa catalyst-precursors were obtained. For instance, the notation of "Cu_5Ga_1" indicates a Cu^{2+} to Ga^{3+} molar ratio of 5:1 was used for synthesizing the catalyst precursor. We also determined the precise Cu/Ga ratio by inductively coupled plasma mass spectrometry (ICP-MS). The ICP-determined Cu/Ga ratios are typically lower than the feed ratio, which is likely resulted from the insufficient doping of Ga during the rapid nucleation and growth of Cu nanoparticles (Supplementary Fig. 1). Note, we chose the sample of Cu_5Ga_1 as the model catalyst for the following discussions owning to its high activity, vide infra.

From the results of scanning electron microscopy (SEM), the introduction of Ga slightly increased the surface roughness of Cu nanoparticles (Supplementary Fig. 2), which is further confirmed by the measurement of electrochemical active surface area (Supplementary Fig. 3). Transmission electron microscope (TEM) images suggest that (Supplementary Fig. 4) both Cu and Cu_5Ga_1 exhibit similar particle size distributions ranging from 20 to 50 nm. Additionally, lattice spacing of 0.18 and 0.21 nm were identified for Cu (200) and Cu (111) in high-resolution TEM (HR-TEM) image of as-prepared Cu sample (Supplementary Fig. 5). Likewise, for the as-prepared Cu_5Ga_1, obvious crystal planes of Cu_2O (110) and (200) with lattice spacing of 0.30 and 0.21 nm, respectively, can be observed on their corresponding HR-TEM images (Fig. 2a). Furthermore, electron energy loss spectroscopy (EELS) mapping (with multiple linear least squares fitting) of the as-prepared Cu_5Ga_1 confirmed the presence of Cu and Ga and their even distributions across the sample particles (Fig. 2a bottom). We also examined the morphology of these catalysts after CO_2R assessments, and observed varying degrees of surface fragmentation in all catalysts. Notably, more pronounced degree of fragmentation and reorganization occurred in the CuGa catalysts, marked by the presence of finely spread small particles (Supplementary Fig. 6). Additionally, post CO_2R, Cu predominately exhibits Cu (111) facet with high crystallinity, as evidenced by HR-TEM images (Supplementary Fig. 7). As for Cu_5Ga_1, a more diverse array of facets, including Cu (200), along with numerous disordered boundaries and defects in addition to the Cu (111) facets, is observable (Fig. 2b). We hypothesize that the introduction of rich boundaries and defects is a result of the Cu-Ga alloying and dealloying process during CO_2 reduction. In general, these rich boundaries and defects are typically recognized as highly active sites for CO_2R, especially for C_{2+} production[54–56]. Furthermore, EELS mapping of post-Cu_5Ga_1 confirmed that the presence of Ga on the catalyst surface (Supplementary Fig. 8).

The powders X-ray diffraction (PXRD) pattern of the as-prepared Cu (Fig. 2c) exhibits three distinctive peaks at 43.4, 50.4, and 74.2°, attributing to Cu (111), (200), and (220), respectively. In contrast, new peaks at 36.5, 42.3, and 61.3° were observed in the as-prepared Cu_5Ga_1 sample. These patterns further confirm the presence of significant amount of oxidized Cu on the surface of Cu_5Ga_1, primarily in the form of Cu_2O (PDF#77-0199). Notably, no apparent characteristic XRD peaks were not identified for Ga, neither metallic Ga nor oxidized forms of Ga. We attribute this to both the low quantity of Ga doping, as well as the atomic dispersions of Ga into the Cu_2O lattices. Similar phenomenon was observed in other related systems[20,35]. X-ray photoelectron spectroscopy (XPS) was employed to reveal the electronic state of Cu of both Cu and Cu_5Ga_1 (Supplementary Fig. 9). As expected, we observed XPS peaks at 952.5 and 932.5 eV corresponding to Cu $2p_{1/2}$ and Cu $2p_{3/2}$, respectively. The shake-up peaks at 945 and 965 eV correspond to the surface native oxide layer of Cu. We analyzed the Cu *LMM* Auger spectra to evaluate the Cu valence state of the bulk samples of Cu and Cu_5Ga_1. As shown in Fig. 2d, no apparent Cu^0 peak was observed in either Cu or Cu_5Ga_1. Besides, the oxidation state of Cu in Cu_5Ga_1 is predominantly +1, lower than that of the as-prepared Cu catalyst (+2). We tentatively attribute this difference to the higher oxophilicity of Ga, preventing Cu in CuGa from being oxidized to CuO under ambient conditions, consistent with the results observed by Raffaella et al.[51]. High-resolution Ga *2p* and Ga *3d* spectra were also collected (Fig. 2e, and Supplementary Fig. 10). Separately, the peak position of Ga 3*d* overlaps with that of K *3p*, a common impurity expected in CO_2R systems. Hence, we collected and analyzed Ga *2p* spectra for more reliable interpretations of the catalyst composition. As shown in Fig. 2e, the two peaks at 1145 and 1119 eV observed for the as-prepared Cu_5Ga_1 can be assigned to Ga $2p_{1/2}$ and Ga $2p_{3/2}$, respectively.

To gather more insights to the valence state and coordination environment of Cu in these two samples, both X-ray adsorption near-edge structure (XANES) and extended X-ray absorption fine structure (EXAFS) were monitored. As shown in Fig. 2f, the Cu *K*-edge features of the as-prepared Cu and Cu_5Ga_1 are closed to the standard samples of CuO and Cu_2O, respectively. Besides, the corresponding Fourier transform of EXAFS spectra (FT-EXAF) indicates a Cu-O bond length close to CuO (~1.49 Å) reference for the as-prepared Cu, and a bond length closer to Cu_2O reference (~1.39 Å) for Cu_5Ga_1 (Fig. 2g), aligning with the above XPS analysis. Additionally, the Ga *K*-edge signal for Cu_5Ga_1 catalyst before and post COR revealed that Ga mostly exists in the form of Ga_2O_3. However, following COR, a new peak at ~2.1 Å appears in FT-EXAF spectra (Fig. 2h), indicating the formation of the bimetallic Cu-Ga composition during electrocatalysis, which we believe will quickly convert to Ga_2O_3 upon cessation of the reaction. Note that, we chose to conduct the *operando* experiment under COR due to its generally high data quality, i.e., no carbonate formation. However, as CO_2 to CO is not the limiting step, we believe the data obtained is relevant for our analysis.

Determining the intrinsic activity of CuGa catalyst towards CO_2R

The as-prepared Cu and Cu_5Ga_1 catalysts were assessed for CO_2R under identical conditions. We first conducted a series of CO_2R measurements under different temperatures to explore the intrinsic activities of these two catalysts toward CO_2R (H-cell, 0.1 M $KHCO_3$, and

https://doi.org/10.1038/s41467-024-51466-8

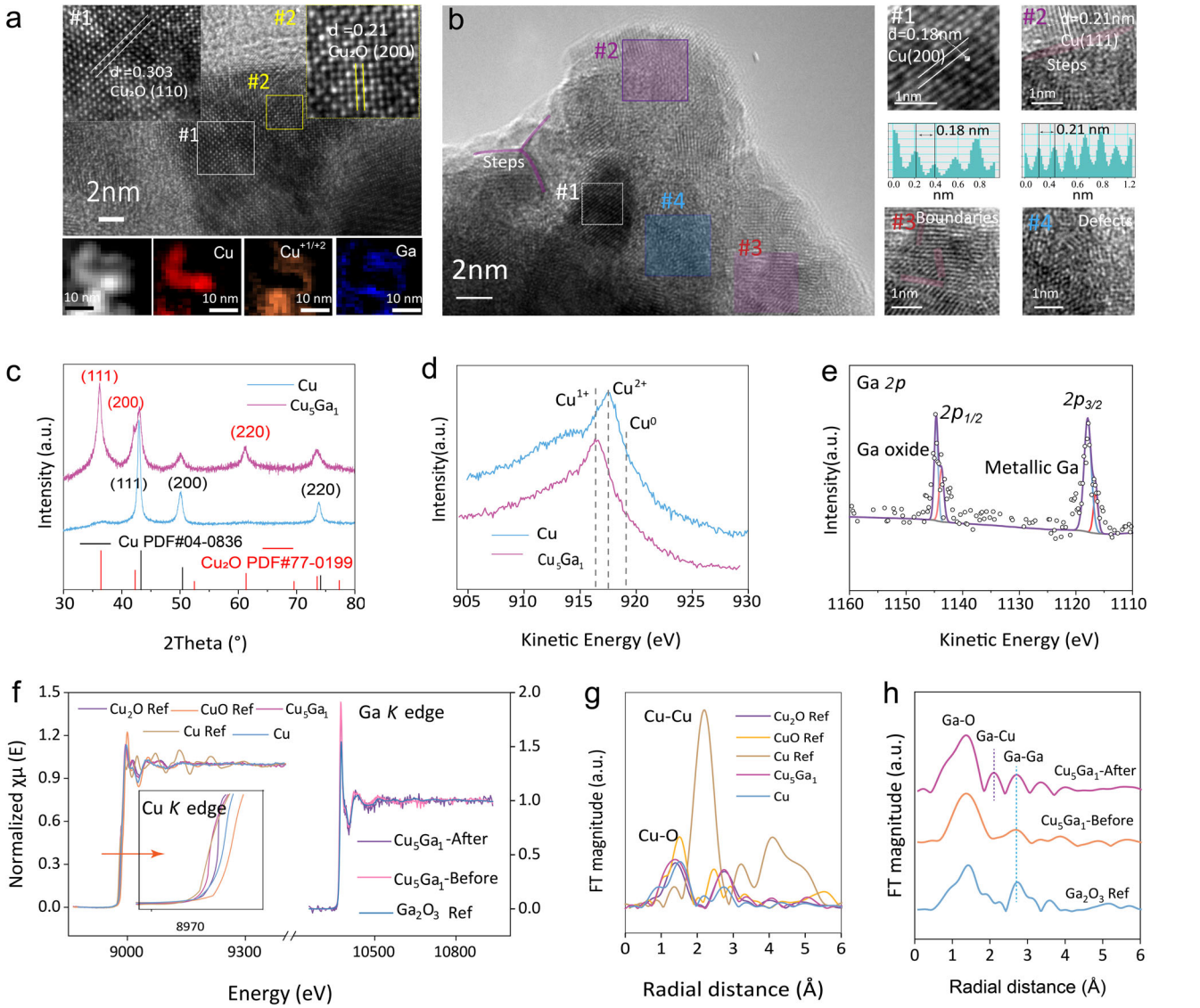

Fig. 2 | Synthesis and characterization of Cu and bimetallic CuGa. HR-TEM images and EELS-mapping of the (**a**) as-prepared and (**b**) post-CO_2R Cu_5Ga_1 catalyst. The PXRD patterns (**c**) and Cu *LMM* Auger XPS spectra (**d**) of as-prepared Cu and Cu_5Ga_1 catalysts. **e** High-resolution Ga *2p* XPS of as-prepared Cu_5Ga_1. **f** Ex-situ XANES at the Cu and Ga *K*-edge of as-prepared Cu and Cu_5Ga_1 catalysts. **g** FT-EXAF spectra at Cu K-edge of Cu and Cu_5Ga_1 catalyst. **h** FT-EXAF at the Ga *K*-edge of the as-prepared and post-catalysis Cu_5Ga_1. Cu foil, Cu_2O, CuO, and Ga_2O_3 are shown as reference. Post-catalysis XAS of $Cu_5Ga_1$was performed immediately after electrocatalytic COR experiment. Relevant source data are provided in the Source Data file.

−1.0V_{RHE}). Note that temperature can affect CO_2 solubility in aqueous electrolyte[57], we thus carefully determined the temperature window to ensure that there were no apparent CO_2 mass transfer limitations, at least at our test potentials (−1.0 V_{RHE}). As shown in Fig. 3a, b, Cu_5Ga_1 exhibits a similar product distribution as Cu, including ethylene (C_2H_4), ethanol (C_2H_5OH), methane (CH_4), formic acid (HCOOH), etc. However, Cu_5Ga_1 demonstrates enhanced selectivity and partial current density towards C_{2+} products and suppressed HER compared to the reference Cu catalyst at all tested temperatures. Furthermore, we plotted the trends of the selectivity, measured in terms of Faraday efficiency (FE) of each product as a function of the electrolyte temperature (Supplementary Fig. 11). We found that the FEs of both H_2 and C_2H_4 decrease as the temperature decreases, while the FEs of CH_4 and C_2H_5OH exhibit the opposite trend. These different trends may result from direct and/or indirect effects of temperature, such as changes in CO coverage, local pH, and surface structure, etc.[58]. As ethylene is the major C_{2+} product, we first plotted the logarithmic dependence of ECSA normalized partial current density of C_2H_4 with reciprocal of temperature to estimate the corresponding activation energy (E_a) based on the Arrhenius equation (2). The same analysis was conducted for H_2 production as it is the major competing reaction.

$$\ln(i) = -\frac{Ea}{R}\left(\frac{1}{T}\right) + \ln(A) \quad (2)$$

where *i* is the partial current density of the specific product, E_a is the corresponding activation energy, *R* is the ideal gas constant, *T* is the reaction temperature, and *A* is the pre-exponential factor[58]. Consequently, as depicted in Fig. 3c, Cu_5Ga_1 exhibits a substantially lower E_a of 28.5 kJ/mol at −1 V_{RHE} towards C_2H_4 production compared to that of Cu (33.1 kJ/mol at −1 V_{RHE}) under identical conditions. Moreover, Cu_5Ga_1 also demonstrates much higher E_a for H_2 production (39.7 kJ/mol at −1 V_{RHE}) compare to that of Cu (27.3 kJ/mol at −1 V_{RHE}, Fig. 3d). Taken together, one can anticipate that Cu_5Ga_1 can inhibit the

https://doi.org/10.1038/s41467-024-51466-8

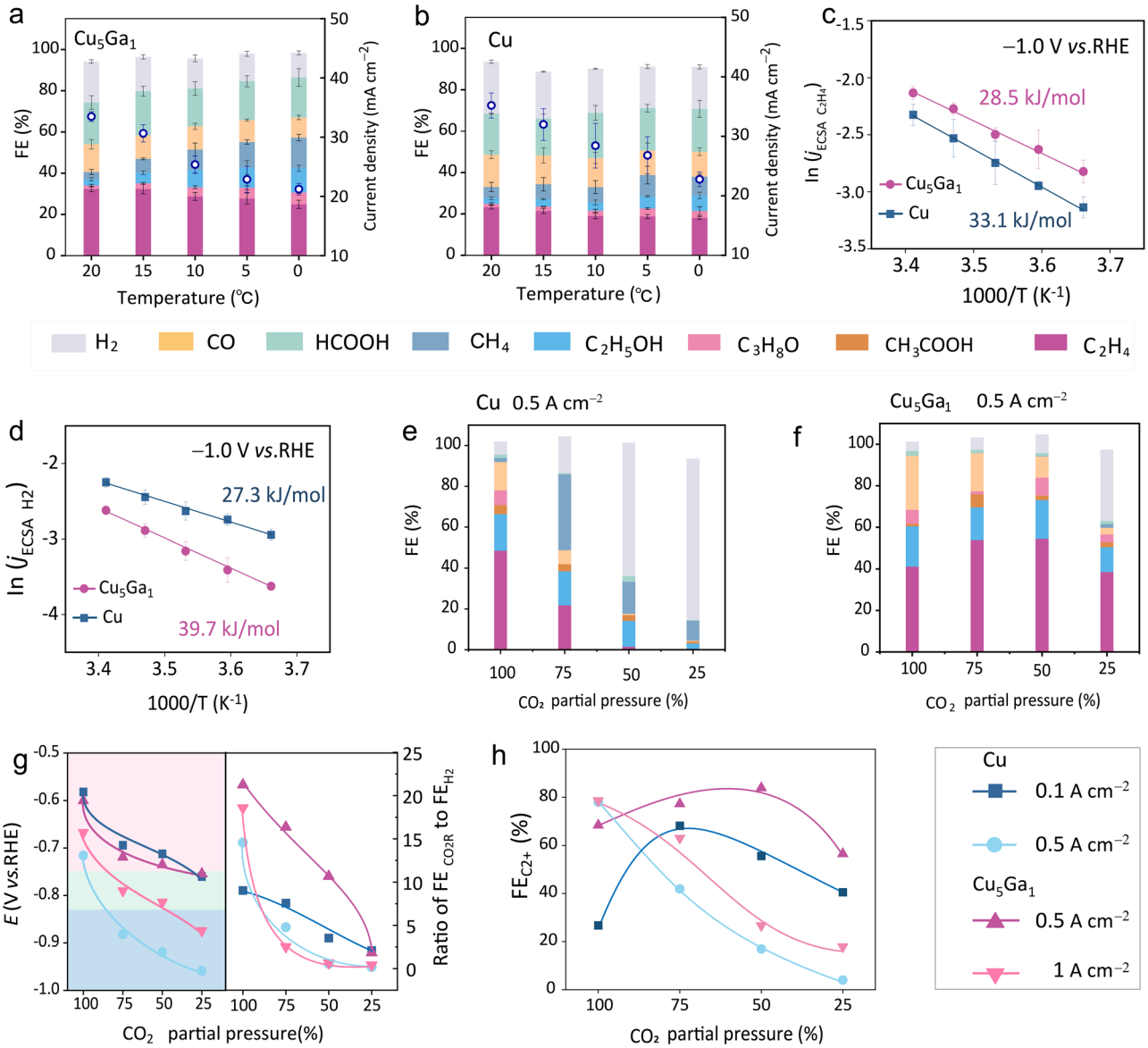

Fig. 3 | Activation energy assessment and CO_2R using CO_2 streams with different partial pressures. CO_2R current densities and FEs for all measurable products at different temperatures at applied potential of −1.0 V_{RHE} in 0.1 M $KHCO_3$ for Cu_5Ga_1 (**a**) and Cu (**b**). **a**, **b** No *iR* correction. The corresponding Arrhenius plots for C_2H_4 (**c**) and H_2 (**d**) productions during CO_2R. The ECSA for Cu and Cu_5Ga_1 in H-cell is 83.4 and 91.3 cm^2, respectively. CO_2R product distribution using different CO_2 partial pressure at current density of 0.5 A cm^{-2} for Cu (**e**) and Cu_5Ga_1 (**f**), measured in flow cell using 1 M KOH as the electrolyte. **g**The applied potential (left) and the ratio of FE_{C2+} to FE_{H2} (right) under different CO_2 partial pressure for CO_2R on Cu and Cu_5Ga_1 under different current density. 100% *iR* correction was applied to calculate the applied potential. The solution resistance (*R*): Cu-100, 3.23 ± 0.9 Ω; Cu-500, 2.61 ± 0.6 Ω; Cu_5Ga_1-500, 2.21 ± 0.8 Ω; Cu_5Ga_1-1000, 2.06 ± 0.4 Ω. Details about the recorded process can be found in the Method section. **h** The FE_{C2+} for CO_2R on Cu and Cu_5Ga_1 catalysts at different current densities with different CO_2 partial pressure. The error bars in **a**–**d** were standard deviations which determined from at least 3 independent experiments. Relevant source data for this figure are provided in the Source Data file.

competing HER during CO_2R and facilitate the production of C_{2+} products, particularly C_2H_4.

To further assess the performance of Cu_5Ga_1 under practical relevant conditions, we conducted CO_2R in a flow cell configuration (Supplementary Fig. 12) and employed diluted CO_2 streams. As shown in Fig. 3e, f, we present the product distributions of Cu_5Ga_1 and Cu at the same current density of 0.5 A cm^{-2}, under different CO_2 partial pressure using N_2 as the inert balance gas. At 100% CO_2 partial pressure, Cu_5Ga_1 (FE = ~68%) exhibits slightly lower C_{2+} selectivity compared to Cu (FE = ~80%), which can be attribute the smaller overpotential applied. However, upon reducing the CO_2 partial pressure from 100% to 75%, the FE_{C2+} of Cu decreased rapidly (to ~40%), coupled with a significant increase in FE_{CH4} (from ~5% to ~30%). This result indicates that flooding likely occurred at the GDE surface. Notably, the applied potential was recorded to be approximately −0.87 V_{RHE} (Fig. 3g left) for Cu at 75% CO_2 partial pressure, aligning with the mass transport region we proposed earlier (Fig. 1b). When we further reduce the CO_2 partial pressure to 50% and 25%, H_2 became the predominate product for Cu, as anticipated (Fig. 3g right). In contrast, Cu_5Ga_1 catalyst exhibits a distinct behavior. Specifically, as the CO_2 partial pressure decreases, the FE_{C2+} increases instead of decreasing, reaching the highest FE_{C2+} (~83%) and FE_{C2H4}(~53%) at 50% CO_2, while the FE_{H2} only increases modestly from 4% to 8%. This intriguing trend further supports our hypothesis on the potential-dependent regions for electrode flooding, as the applied potential for Cu_5Ga_1 is only −0.7 V_{RHE} at 50% CO_2. When we further reduce the CO_2 partial pressure to

25%, the applied potential increased significantly to compensate for the CO_2 concentration overpotential. Consequently, we observed a significant decrease in FE_{C2+} (~60%), and increase in selectivity towards to CH_4 and H_2, indicative of flooding at the GDE reaction layer.

To further validate the hypothesis on the potential-dependent electrode flooding behavior, we varied the applied potential for both Cu and Cu_5Ga_1 based on our preliminary categorization of different kinetic regions (Fig. 1b). As shown in Fig. 3g, we chose current densities of 0.1 and 0.5 A cm^{-2} for Cu, and current densities of 0.5 and 1 A cm^{-2} for Cu_5Ga_1 for this assessment, respectively. At the current density of 0.1 A cm^{-2}, applied potentials for Cu at different CO_2 partial pressure lie in the kinetic and mixed-control region, indicating flooding may not occur significantly. These applied potentials are similar to those applied to Cu_5Ga_1 at 0.5 A cm^{-2}, as anticipated, we observed similar trends in the ratio of CO_2R/HER (Fig. 3g right) and the changes of FE_{C2+} (Fig. 3h and Supplementary Fig. 13). To drive a higher current density, as depicted in Fig. 3g, the applied potentials for both Cu_5Ga_1(1 A cm^{-2}) and Cu (0.5 A cm^{-2}) quickly enter the mixed-control region (negative than −0.75 V_{RHE}) and then the severely flooded region as CO_2 partial pressure decreases. As expected, we observed a rapid decrease in both the ratio of FE_{CO2R}/FE_{H2} and the overall FE_{C2+} (Fig. 3g, h). These correlations indicate that the GDE reaction interface stability regarding flooding is most likely related to applied potential. Taken together, our results suggested that the introduction of Ga can significantly reduce the activation overpotential for the production of C_{2+} products, e.g., C_2H_4, and inhibit HER process. Benefiting from the reduced activation overpotential, the overall applied cathodic potential is sufficiently low in the case of Cu_5Ga_1 for achieving high current density for C_{2+} production while preventing sever electrode flooding.

Exploring the origin of improved activity of the CuGa catalyst

In addition to the morphological changes (Fig. 2d), we also observed that the presence of the Ga exhibits a noticeable effect on preventing Cu oxidation under ambient conditions, as evidenced by XRD, Cu 2*p* XPS, and Cu *LMM* Auger results (Supplementary Figs. 14 and 15). We believe this effect is likely due to the high oxophilicity and low electronegativity of Ga. Furthermore, we observed a substantial loss of Ga from the CuGa catalysts after CO_2R, as evidenced by EELS fitting, Ga 2*p* XPS, and ICP-MS (Supplementary Figs. 8, 16, and 17). We propose that the Ga loss can be attributed to two factors. Firstly, it may occur during the alloying–dealloying process. Secondly, the hydrophobicity of the GDE electrode decreases upon reaction cessation, leading to the etching of the Ga_2O_3 layer by KOH. Nevertheless, we believe the residual minor Ga on the catalyst surface could still play a significant role during catalysis. We will delve into a detailed discussion on this aspect thereinafter.

We also investigated the dynamic changes in Cu and CuGa catalysts under working conditions by in-situ XANES. Due to the insufficient signal-to-noise ratio caused by interfacial instability in alkaline CO_2R reaction (i.e., carbonate formation) under practical relevant current densities, we opted to perform COR instead of CO_2R, since the CO_2 to CO step is most likely not the limiting step on both Cu and CuGa in our experimental conditions[59]. As shown in Fig. 4a, the Cu *K*-edge normalized absorption spectra of Cu_5Ga_1 and Cu catalysts at the OCV state reveal that in the as prepared Cu_5Ga_1 sample, Cu exists predominately in the state of Cu_2O, whereas in the as synthesized Cu catalyst, it mostly exists in the state of CuO (Supplementary Fig. 18). Upon the application of a negative potential to initiate the COR, the Cu matrix of both catalysts undergoes a swift conversion from oxidized states to the metallic state during electrocatalysis. While previous reports suggest that the presence of Cu^{+1} can promote C_2H_4 selectivity and stability[60,61], there is insufficient evidence to support the notion that Ga can help maintain the +1-oxidation state in our system. As depicted in Fig. 4b, FT-EXAF conversion reveals that at applied negative potentials (−0.48, and −0.63 V_{RHE}), the length of Cu-Cu bond in Cu_5Ga_1 (~2.25 Å) slightly exceeds that of the standard Cu foil (~2.18 Å). As the potential becomes more negative, the Cu-Cu bond length returns to the standard length. However, obtaining high-quality in-situ signals for the Ga *K*-edge was not successful due to its low content and significant background fluorescence interference from Cu[35,62]. Nonetheless, Cu-Ga bond can be clearly observed in the same measurement after COR reduction (Fig. 2h). Taking into account the theoretical potentials for Ga^{3+}/Ga^0 (EGa_2O_3/Ga^0 = −0.485 V_{RHE}, $EGaOOH/Ga^0$ = −0.493 V_{RHE}, $EGa(OH)3/Ga^0$ = −0.415 V_{RHE})[63] and the above results, we reasonably speculate that the above potential-dependent change in Cu-Cu bond length is a result of alloying and dealloying processes. We believe that Ga tends to redeposit onto the Cu lattice during catalysis, consistent with similar observations made elsewhere[51].

Attenuated total reflection surface-enhanced infrared absorption spectroscopy (ATR-SEIRAS) was employed to monitor adsorption behavior of *CO, a key intermediate for CO_2/COR reaction. Previous work has suggested that the CO_2 to CO steps is not rate-limiting on Cu for C_{2+} products[59]. Therefore, to eliminate the influence from the CO_2 to CO steps, we carried out IR measurements directly under the COR conditions to monitor the *CO on Cu_5Ga_1 and Cu, ensuring a fair comparison. As shown in Supplementary Fig. 19a, b, as the cathodic potential increases from OCV, a distinct band in the range of 2000 -2100 cm^{-1}, attributed to the atop-bound CO (CO_{ad}) on the catalyst surface, emerged on both Cu_5Ga_1 and Cu. Note, the observed CO_{ad} peak are well described by a commonly used model consisting of the "low frequency band" and the "high frequency band" (Fig. 4c, d)[64,65]. Assuming Beer's law holds, the integrated CO_{ad} peak area is directly proportional to the CO_{ad} coverage[66]. In this case, one could observe that the CO_{ad} coverage on Cu_5Ga_1 is higher than that of Cu (Supplementary Fig. 19c). Noted, other factors, such as surface enhancement efficiency, ECSA of catalysts, etc., will also affect this high "CO_{ad} peak area". On the other hand, the wavenumber of CO_{ad} is more closely associated with the CO_{ad} binding strength on a given catalyst[67]. As a result, we observed that the wavenumbers of both CO_{ad} peaks on Cu_5Ga_1 consistently remain slightly higher than those on Cu (Supplementary Fig. 19d), indicating that the binding strength of CO_{ad} on Cu_5Ga_1 is slightly lower than on the pristine Cu.

To further understand the effect of CO adsorptions, we analyzed CO generation during CO_2R and found that Cu_5Ga_1 indeed exhibited substantially higher selectivity and partial current density towards CO, particularly at low potentials compared to Cu (Supplementary Fig. 20). As shown in Fig. 4e, Cu_5Ga_1 consistently exhibits a higher partial current density (CO and C_{2+} combined) than that of Cu across a broad overpotential window, even when normalized to its higher ECSA. Given the minimal production of CH_4 and HCOOH, we believe this enhanced intrinsic activity of Cu_5Ga_1 is most likely resulted from its weaker CO_{ad} binding strength and more favorable CO_{ad} activation coupling step.

We then conducted density function theoretical (DFT) calculations on CuGa catalyst to further understand the improved intrinsic activity of the bimetallic CuGa catalyst. The corresponding optimized computational model structure of Ga on Cu (100) are provided in Supplementary Data 1. Despite the experimentally determined Ga/Cu ratio in post-Cu_5Ga being ~1:20, we found that Ga doping at the topmost layer is energetically favored by 0.43 eV than at the subsurface, which is substantial. Therefore, a higher Ga concentration on the surface of CuGa catalysts should be expected. However, determining the actual coverage of Ga is challenging. Alternatively, we have considered four different Ga coverages on Cu surface: 0.0 ML, 1/6 ML, 1/4 ML, and 1/2 ML. On the pristine Cu (100) surface, we found that CO prefers to be adsorbed on the hollow site, which is more stable by 0.06 eV than the bridge site, and by 0.13 eV than the atop site. The calculated free energy barrier for CO-CO coupling is 0.76 eV, aligning well with the previous calculations[68]. In a recent work, the Ga-doping on Cu(111) surface was found to promote the CO adsorption[52]. We found that CO adsorption at the Ga site on Cu (100) is suppressed rather than promoted. The adsorption energy of CO at the Ga site was calculated to be 0.86 eV

https://doi.org/10.1038/s41467-024-51466-8

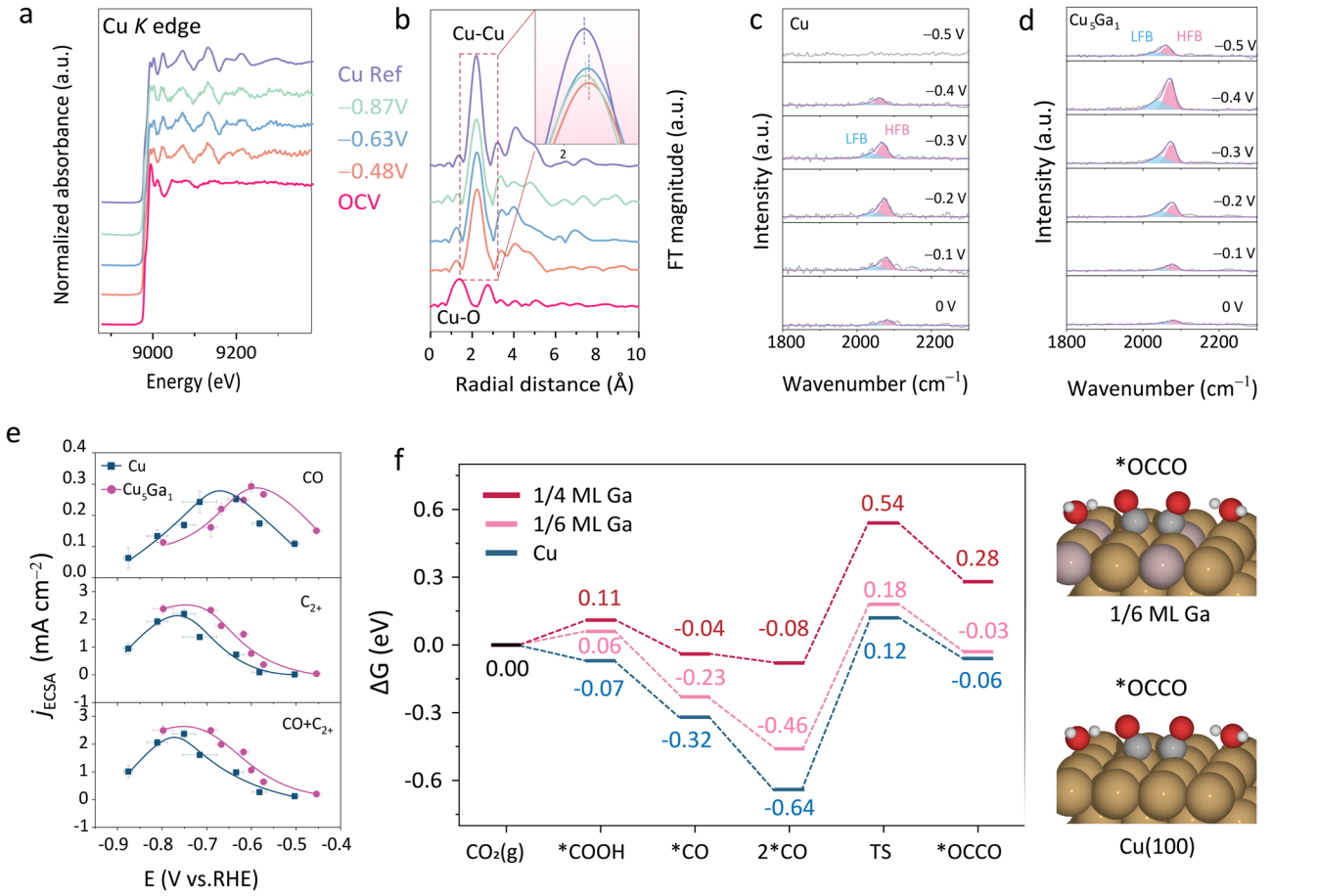

Fig. 4 | In-situ characterization of Cu and Cu_5Ga_1 during CO/CO_2R. a In-situ XANES at the Cu *K*-edge of Cu_5Ga_1 catalysts during COR condition (1 M KOH, flow cell) with different applied potentials. 100% *iR* (4.3 ± 0.3 Ω) correction was applied to calculate the applied potential. **b** the corresponding FT-EXAF spectra at Cu *K*-edge of Cu_5Ga_1 catalyst. Cu foil is shown as reference. In-situ ATR-SEIRAS spectra of Cu (**c**) and Cu_5Ga_1 (**d**) during COR at different applied potentials. 100% *iR* correction was applied to calculate the applied potential. The solution resistance (*R*) for Cu and Cu_5Ga_1 is18.2 and 10.2 Ω, respectively. **e** Potential-dependent CO_{ad} peak area on Cu and Cu_5Ga_1 in in-situ ATR-SEIRAS spectra. **e** The partial current density of CO (top), C_{2+} products(middle), and its sum (bottom) in CO_2R reduction (1 M KOH, flow cell) under different applied potential. 100% *iR* correction was applied to calculate the applied potential. The solution resistance (*R*) for above analysis can be found in figure caption of supplementary Fig. S22. Details about the recorded process can be found in the Method section. **f** The free energy surface (FES) for CO_2 reduction to CO and CO-CO coupling with Cu (100) surface with 0.0, 1/6, and 1/4 ML of Ga. Right sides are the structures of the *OCCO on the1/6 ML Ga and pristine Cu (100). Atom color code: Cu, dark yellow; Ga, light purple; C, black; O, red; H, white. Relevant source data are provided in the Source Data file.

higher than that of at the Cu atop site on the pristine Cu (100) surface. Additionally, after structural optimization, all the CO molecules initially placed at the Cu-Ga bridge site or the 3Cu-Ga hollow site will diffuse to the Cu atop site. Therefore, the most favorable adsorption site for CO is expected to vary with the Ga coverage. With 1/6 ML Ga, CO can still park at hollow sites that are not adjacent to Ga. However, with 1/4 ML and 1/2 ML Ga, the hollow site becomes coordinated to at least one Ga atom, making the atop site becomes the favorable site for CO adsorption. In all, as the Ga coverage increases, we found a weakening in the adsorption of all the reaction intermediates (Fig. 4f). For instance, the adsorption free energy of CO on the pristine Cu (100) surface is −0.32 eV, and it is weakened to −0.23 eV, −0.04 eV, and 0.12 eV with 1/6 ML, 1/4 ML, and 1/2 ML of Ga, respectively. Besides, Bader charge analysis reveals that each Ga atom doped on Cu (100) surface will donate about 0.22 electrons to the surrounding Cu atoms due to the lower electronegativity of Ga compared to Cu. It has been previously demonstrated that the interaction between CO and Cu is governed by both the π-bonding and σ-repulsion[69], with the latter being sensitive to the occupancy of Cu sp-band. Consequently, the electrons donated by Ga occupy more Cu sp-bands, resulting in higher σ-repulsion and, therefore, weaker CO adsorption.

Owning to the weakening of CO adsorption, the free energy surfaces suggest that the surface can efficiently reduce CO_2 to CO (Fig. 4f, Supplementary Fig. 21). As a result, we found that the effective barriers for CO-CO coupling to form OCCO are substantially lowered upon Ga-doping. Specifically, the reaction barriers are reduced by 0.08 eV, 0.10 eV, and 0.05 eV with Ga coverages of 1/6 ML, 1/4 ML, and 1/2 ML, respectively, suggesting that Ga-doping can promote the formation of C_{2+} products across a wide range of Ga coverages. We believe the weakened adsorption of CO leads to reduced activation energy required for reaching the transition state for CO-CO coupling or forming other activated CO states, resulting in enhanced activity towards C_{2+} products as we observed experimentally.

Energy efficiency assessment of CO_2/COR on Cu_5Ga_1

After pinpointing the enhanced activity of the CuGa catalysts, we proceeded to validate its performance for CO_2/COR reaction in more practical relevant reactors. We first analyzed the product distributions for both CO_2R and COR on CuGa (Supplementary Figs. 22–27) and compared them to those observed on pristine Cu to investigate the effect of Ga-doping on C_{2+} products selectivity. As shown in Supplementary Figs. 26, 27, we observed similar products distributions,

https://doi.org/10.1038/s41467-024-51466-8

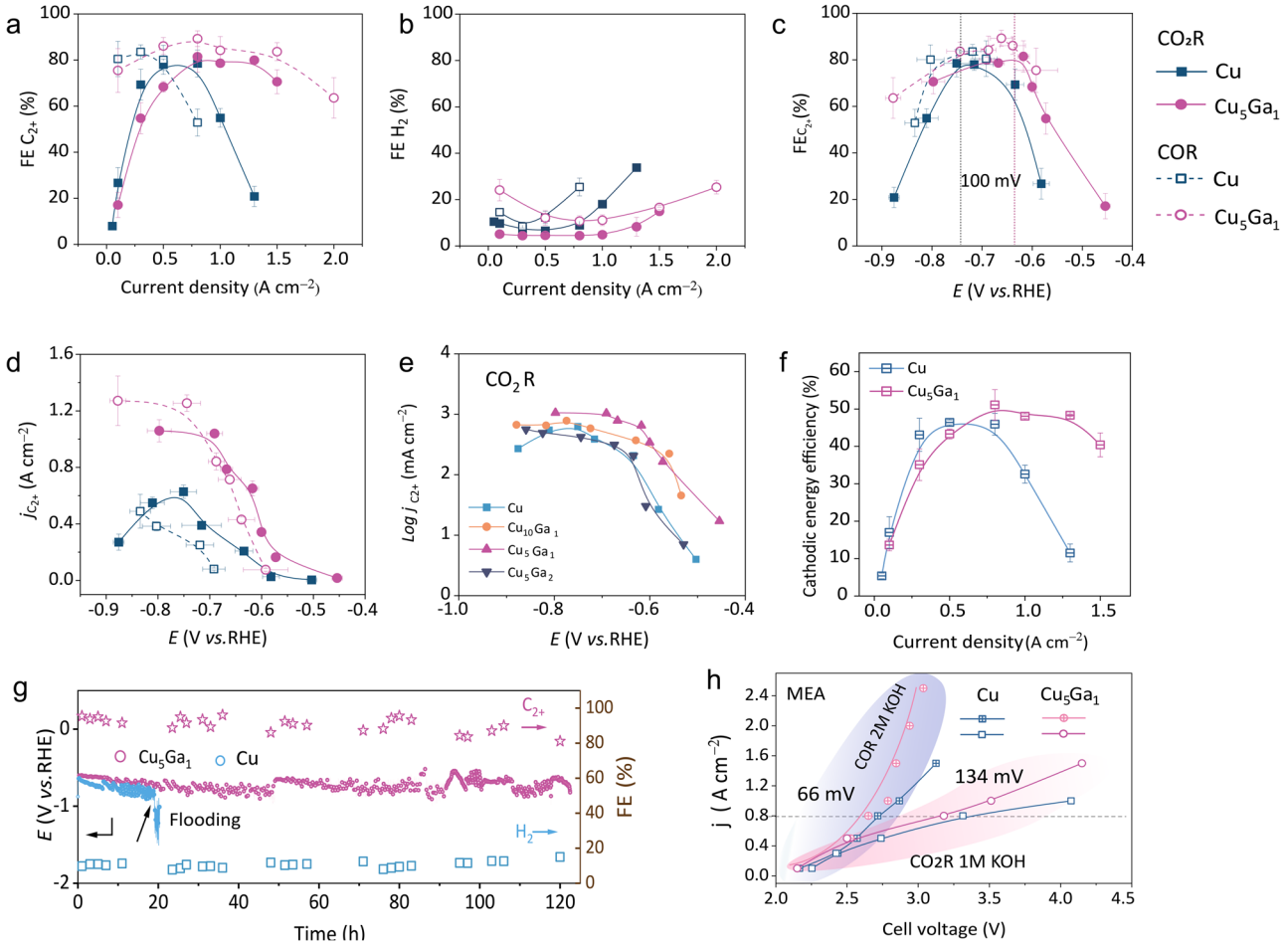

Fig. 5 | Energy efficiency analysis of Cu and Cu_5Ga_1 during CO/CO_2R. The FE_{C2+} (**a**), FE_{H2} (**b**) of Cu and Cu_5Ga_1 in CO_2 (solid) and COR (hollow). **c** The FE C_{2+} distribution of two catalysts at different applied potentials in CO_2/COR. **d** Partial current densities of C_{2+} products of Cu and Cu_5Ga_1 in CO_2 /COR. **e** The normalized partial current density of C_{2+} as function of applied potentials for four catalysts in CO_2R. **f** The $EE_{1/2}$ for two catalysts at different current density under CO_2R. **a**–**e** The CO_2/COR tests were performed in flow cell with 1 M KOH as electrolyte, Ni foam as counter electrode, and the flow rate of electrolyte and CO_2/CO feeding is 25 mL/min. **g** Stability test at −0.3 A cm^{-2} current density in flow cell for Cu and Cu_5Ga_1, the anode electrolyte was regularly renewed. **a**–**g** 100% *iR* correction was applied to calculate the applied potential. The solution resistance (*R*) for above analysis can be found in figure caption of supplementary Figs. S22 and S23. Details about the recorded process can be found in the Method section. **h** The current density for two catalysts at different cell voltages; purple area for COR with 2 M KOH as anode electrolyte; pink area for CO_2R with 1 M KOH as anode electrolyte. **h** The CO_2/COR tests were performed in MEA with different electrolytes, IrO_x/Ti mesh as counter electrode, and the flow rate of CO_2/CO is 25 mL/min. The error bars in a-f were standard deviations which determined from at least 3 independent experiments. Relevant source data are provided in the Source Data file.

i.e., ethylene-to-oxygenates ratios, on both Cu_5Ga_1 and Cu, for both CO_2R and COR before flooding occurs. However, as the current density increased, this ratio on Cu_5Ga_1 only increased slightly, while the ratio on pristine Cu increased dramatically due to the decrease in liquid products. This is likely induced by electrolyte flooding caused by the rapidly increased cathodic potential for the pristine Cu. Separately, favored liquid C_{2+} products (~50%), especially for acetate (~20%), were observed in COR compared to CO_2R (liquid C_{2+} products ~30%, acetate ~5%) on both CuGa and Cu. We believe this observation is likely attributed to the higher local pH and CO partial pressure during COR (Supplementary Note 1, Supplementary Table 4)[70]. Taken together, we believe that Ga-doping into Cu predominately facilitates the kinetic rate-limiting step (*CO activation) and consequently enhances the overall C_{2+} production activity. As this kinetic rate-limiting step precedes the selectivity-determining step for C_{2+} production, we did not observe an obvious difference in terms of C_{2+} selectivity and ethylene-to-oxygenate ratios between CuGa and Cu, for both CO_2R and COR. Consequently, as shown in Fig. 5a, the optimal CuGa catalyst (Cu_5Ga_1) achieves high FE_{C2+} (> 80%) and low FE_{H2} (<~5%) (Fig. 5b) across a wide current density range of 0.8–1.3 A cm^{-2} in CO_2R. The excellent performance of Cu_5Ga_1 is even more pronounced in COR, achieving more than 85% FE_{C2+} selectivity in the wide current density range of 0.5–1.5 A cm^{-2}. Furthermore, we also found that, for both CO_2/COR, CuGa catalysts achieve the highest FE_{C2+} at much lower overpotential compared to Cu. Notably, the decrease in overpotential is more pronounced in the case of COR. For instance, at small current densities (0.1–0.3 A cm^{-2}) where flooding may not occur, or at least not severely, the reduction in overpotentials already exceeds 100 mV. (Fig. 5c, Supplementary Fig. 28).

Our attention also extended to the production of H_2 and CH_4, two representative indictors of interface instability in Cu-based systems[71]. We found that ~ −0.75 V_{RHE} emerged as a turning point in our measurements for both CO_2/COR (Fig. 5d, Supplementary Figs. 29–31). When the applied potential went below ~ −0.75 V_{RHE}, both the FE_{H2} and FE_{CH4} quickly increased for all catalysts in both CO_2/COR, indicating flooding occurred at the reaction interface. Additionally, the ratios of FE_{C2+} to FE_{C1+} (C_1 includes both CO and CH_4) at different potentials also exhibit the same trends (Supplementary Fig. 32). Overall, these observations align well with our hypothesis on potential-dependent electrode-flooding behavior, and the high intrinsic activity of CuGa catalysts ensures substantially enhanced current density can be

achieved with sufficiently low cathodic potentials (Fig. 5e, Supplementary Figs. 33, 34). As a result, showing in Fig. 5f, Cu_5Ga_1 achieves an encouragingly high cathodic EE of >50% towards C_{2+} products at a high current density of 1 A cm^{-2}, surpassing that of Cu (~30%) significantly. Even at a further increased current of 1.5 A cm^{-2}, Cu_5Ga_1 maintained over 40% cathodic $EE_{1/2}$ for C_{2+} products, while that of Cu rapidly dropped to less than 10%.

Single-pass carbon conversion efficiency (SPCE) serves as another crucial indicator for evaluating the CO_2R performance. To mitigate the severe CO_2 loss in alkaline electrolyte, we assessed the CO_2R performance and SPCE in acidic electrolytes (0.5 M K_2SO_4, pH = 2). As anticipated, Cu_5Ga_1 catalyst demonstrated substantially higher C_{2+} selectivity and lower overpotential at all current densities compared to those observed on Cu, confirming its enhanced performance observed in alkaline CO_2R (Supplementary Fig. 35). Furthermore, at the optimal CO_2 flow rate, an appreciable SPCE of 40% could be achieved at a current density of 500 mA cm^{-2} in Cu_5Ga_1-based CO_2R in acidic electrolyte.

Stability is equally crucial for $CO_{(2)}R$. In the CO_2R, Cu GDE rapidly flooded due to the higher cathodic potential required for 0.5 A cm^{-2}, while the Cu_5Ga_1 GDE could last for significantly longer time under the identical operating current density (Supplementary Fig. 36). Considering that salt crystallization in the CO_2R also contributes to destabilize of the GDE reaction interface. Hence, we focused on assessing the impact of electrode potential on the stability of COR (Fig. 5g). The results revealed that the Cu_5Ga_1-GDE can maintain ~90% FE_{C2+} at an industrial current density (0.3 A cm^{-2}) for more than 120 h, while the Cu-GDE experiences system failure at ~20 h. Cu-based catalysts may undergo degradations due to dissolution, restructuring, and fermentations, which can lead to unsatisfactory stability for long-term COR electrolysis[72,73]. Therefore, to explore the origin of the instability of pristine Cu electrode, we carried out detailed analysis on the changes in ECSA, product distributions, and OH^- adsorption of the two catalysts during and after COR for various time periods (Supplementary Figs. 37–39). As a result, we conclude that the electrolyte flooding is the predominant cause of the instability of pristine Cu during long-term COR electrolysis, despite a certain level of surface restructuring occurring in both catalysts.

We proceeded to assemble a MEA reactor to minimize the ohmic overpotential and assess the performance of CuGa catalysts for CO_2/COR by using different anode electrolytes. In the CO_2R reaction, resembled those obtained in the flow-cell, the Cu_5Ga_1 catalyst demonstrated a low cell voltage towards CO_2R products than that of Cu. Specifically, at a current density of 0.8 A cm^{-2}, the cell voltage observed in Cu_5Ga_1-MEA was ~134 mV and 247 mV lower compared to those of Cu-MEA, in 0.1 M $KHCO_3$ and 1 M KOH, respectively (Fig. 5h, Supplementary Figs. 40–43). In the COR reaction, both Cu and Cu_5Ga_1 exhibited enhanced activity compared to CO_2R and achieved higher FE_{C2+} (~90%) across a wide current density range of 0.1–1.5 A cm^{-2} (Supplementary Fig. 44). More remarkably, benefiting from the lower cell voltage, Cu_5Ga_1 catalyst can achieve a high current density of 2.5 A cm^{-2} at a cell voltage of 3 V and still maintaining a ~70% FE_{C2+} (with a partial current density of C_{2+} of 1.6 A cm^{-2}). As expected, the highest EE (~40%) of Cu_5Ga_1 in COR can be achieved at 0.8 A cm^{-2}, and it can maintain ~30% at high current density (2 A cm^{-2}). In contrast, Cu-MEA will quickly shift to the HER due to system instability at current densities exceeding 1.5 A cm^{-2}. As for the EE in CO_2R, Cu_5Ga_1 also maintains high full-cell EE at larger current densities, compared to Cu (Supplementary Fig. 45). Additionally, upon comparing the $EE_{1/2}$ and full-cell EE achieved in the flow cell and MEA with the latest research results, we found that the Cu_5Ga_1 catalyst in this study demonstrated advantages in energy efficiency especially at high current densities (Supplementary Fig. 46 and Tables 5, 6).

Discussion

In conclusion, we observed that the currently low energy efficiency for $CO_{(2)}R$ is largely resulted from the high concentration overpotentials induced by GDE instability (i.e., flooding issue), particularly when under high cathodic potential is applied to drive high current density. To mitigate this challenge, we developed a bimetallic CuGa catalyst with a reduced activation overpotential for producing C_{2+} products. This improvement is attributed to the combination of the electronic effect of Ga doping and the resulting undercoordinated Cu sites during catalysis. As a result, the Cu-Ga based GDEs could achieve substantially high $CO_{(2)}R$ current density with sufficiently low overpotentials. This low overpotential, in turn, enables the energy-efficient and stable operation of $CO_{(2)}R$ at high current densities. For instance, using the optimized Cu_5Ga_1 catalyst, we the achieved over 50% cathodic energy efficiency towards C_{2+} at a high current density exceeding 1.0 A cm^{-2}. Moreover, when employing this Cu_5Ga_1 catalyst in a MEA reactor, a notable COR current density of 2 A cm^{-2} was realized at a modest cell voltage of 3 V, corresponding to a full cell energy efficiency of over 30%. Overall, the correlation between the electrode potential and the stability of the reaction interface, along with the strategy proposed in this study, opens a pathway for the energy-efficient electrosynthesis of C_{2+} products from CO_2/CO.

Methods

Chemicals

Copper (II) chloride dihydrate ($CuCl_2 \cdot 2H_2O$, ≥99.0%), sodium borohydride ($NaBH_4$, 99.99%), hydrochloric acid (HCl, GR), Gallium (III) oxide (Ga_2O_3, 99.99%), Polytetrafluoroethylene solution (PTFE, 60 wt%) and isopropyl alcohol (IPA, 99.5%), Nafion™ D520 (5 wt% in EtOH) were purchased from Sigma-Aldrich. All chemicals were used without further purification. Gallium chloride ($GaCl_3$, 99.99%), potassium hydroxide (KOH, 99.99%), potassium bicarbonate ($KHCO_3$, 99.99%) were purchased from Macklin. Anion-exchange membrane (Sustainion X37-50 RT Grade) was purchased from Dioxide Materials. The carbon paper with microporous Layer (YLS-30T), pure carbon paper (TGP-H-060), and IrOx/Ti mesh were purchased from Suzhou Sinero Technology company. All chemicals were used as received. Ultra-pure water (18.2 MΩ. Cm, Millipore) was used throughout the experiments.

Characterizations

Ex-situ characterization. The surface morphology of as-prepared and post reaction catalysts were characterized by field scanning electron microscopy (FE-SEM, SU-8000, Hitachi, Tokyo). Transmission electron microscopy (TEM) image and EELS mapping were obtained by JEOL JEM-2010F (Japan). X-ray diffractometer (XRD, Bruker D8-advance) was applied to characterize the crystal structure with a Cu K-α as X-ray source. X-ray photoelectron spectroscopy (XPS) was conducted to analysis the surface chemical compositions on an Escalab 250 Xi (America) with an Axis Ultra DLD spectrometer (resolution 0.5 eV). In-situ ATR-SEIRAS spectra during COR at different applied potentials (0.5 M $KHCO_3$ as the electrolyte) was measured by Fourier transform infrared spectroscopy (FTIR, IRTracer-100, Shimadzu).

The catalysts were dropped on a gold-coated silicon table as a working electrode. *Ex*-XAS and in-situ XAS were performed at XAFCA beamline of Singapore Synchrotron Light Source under transmission/fluorescence mode. Cu and Ga *K*-edge XANES spectra were collected. Athena was used for data process. Inductively coupled plasma optical emission spectroscopy (ICP-OES, Thermo Scientific™ iCAP™ 7400) analysis was applied to quantify the mass of Cu and Ga on the electrodes.

Catalysts synthesis

The Cu and CuGa presuors were synthesized via one-step reduction process. Specifically, the Cu_5Ga_1 was synthesized as follows. The reduction solution was first prepared, including 378.3 mg $NaBH_4$ and 10 mL H_2O. And then prepared the CuGa precursor solution, dissolved 255.0 mg of $CuCl_2 \cdot 2H_2O$ in 3 mL of dilute hydrochloric acid (2 M), and then add 1 mL of $GaCl_3$ (0.3 M) solution. The resulting mixed CuGa

solution was sonicated for 5 min and then added dropwise to the $NaBH_4$ reduction solution in an ice bath. After stirring for 1 h, the black solid is collected by centrifugation, washed with ultrapure water and IPA, and dried in a vacuum oven at 60 °C. To obtain $Cu_{10}Ga_1$ and Cu_5Ga_2, the add volumes of $GaCl_3$ solution were 0.5 and 2 mL, respectively. Cu was obtained without $GaCl_3$ solution. The other steps were same to the synthesis procedure of Cu_5Ga_1.

Electrochemical measurements

All electrochemical tests were performed using BioLogic VMP3 with a 10 A booster (equipped with a built-in EIS analyzer). The solution resistance (R) in both H-cell and flow cell was evaluated using potentiostatic electrochemical impedance spectroscopy (PEIS). PEIS measurements were conducted before and after the $CO_{(2)}R$, with a frequency scan range from 1 MHz to 10 Hz. The resulting data were analyzed using EC-Lab software. In the PEIS results, the intersections of the Nyquist plot with the x-axis at the high frequency regions were used to estimate the corresponding solution resistance. All the potential were recorded against Ag/AgCl and then converted to reversible hydrogen electrode (RHE) with *iR* compensation following the equation below:

$$E(\upsilon s.\mathrm{RHE}) = E\left(\mathrm{vs.}\frac{\mathrm{Ag}}{\mathrm{AgCl}}\right) + 0.197\mathrm{V} + 0.0591\mathrm{V} \times \mathrm{pH} - iR \qquad (3)$$

For the $CO_{(2)}R$ tests conducted in both H-cell and flow-cell setups, the solution resistance at each applied potential was measured before and after electrolysis to ensure 100% *iR* compensation. In the membrane electrode assembly (MEA) setup, the full cell voltage was recorded without *iR* correction.

The Ag/AgCl reference electrode was calibrated using a reversible hydrogen electrode (RHE) in a high-purity H_2-saturated 0.5 M H_2SO_4 electrolyte (pH = 0), with a Pt wire as the working electrode and a graphite rod as the counter electrode. Cyclic voltammetry (CV) was conducted at a scan rate of 1 mV/s, and the thermodynamic potential for the hydrogen evolution reaction (E = 0 V *vs.* RHE) was determined as the average of the two potentials where the current was zero. The above calibration resulted in a measured RHE value of −0.197 V *vs.* Ag/AgCl. Hence, −0.197 V was used for converting the applied cathodic potentials to RHE in our experiments.

Different electrolytes were employed in this study. For the H-cell, 0.1/0.5 M $KHCO_3$ was used. For flow-cell tests, the electrolytes included 1 M KOH, 0.5 M K_2SO_4 (acidic, H_2SO_4 was used to adjust pH to 2), and 1 M $KHCO_3$ (neutral). For the MEA tests, 0.1 M $KHCO_3$, a 1 M KOH, and 2 M KOH served as neutral and alkaline electrolytes, respectively. Fresh electrolytes were prepared by dissolving the appropriate amounts of KOH, K_2SO_4, and $KHCO_3$ in 1 L of ultrapure water, stored in a sealed polypropylene bottle. The pH of the solutions was measured using a Mettler-Toledo S400 benchtop pH meter, with the pH values of 0.1 M $KHCO_3$ (CO_2 saturated), 0.5 M $KHCO_3$ (CO_2 saturated), 1 M KOH, and 2 M KOH being 6.81 ± 0.03, 8.3 ± 0.05, 14.10 ± 0.03, and 14.35 ± 0.05, respectively.

Gaseous products were analyzed and quantified using gas chromatograph (GC, Shimadzu 2014), with the actual gas flow rates, measured by a bubble flowmeter, at the inlet of GC (after outlet of the CO_2R reactor) for gaseous product quantification for each single experiments. On the other hand, liquid $CO_{(2)}R$ products were analyzed and quantified by ^{1}H NMR spectrum (Bruker 400 MHZ system) using DMSO and Phenol as the internal standard.

Temperature dependent CO_2R experiments

These experiments were performed in a H-Cell purchased from GaossUnion using 0.1 M $KHCO_3$ as the electrolyte. The working electrode (carbon paper, TGP-H-060) in the H-cell was prepared by the drop-coating method. Specially, the catalyst ink was prepared by dispersing 1 mg of catalyst in 1 mL mixture solution (with a water and isopropyl alcohol ratio of 7:3) containing 5 µL of Nafion, followed by thorough ultrasonication. Then, the resulted catalyst ink was coated on the carbon paper (TGP-H-060) with an active area of 1 cm^2. The catalyst mass loadings were estimated to be ~1 mg/cm^2 by weighing the carbon paper electrodes before and after the catalyst loading after drying. Besides, Pt foil and Ag/AgCl were employed as the reference electrode and counter electrode in the H-cell, respectively. AEM (Sustainion X37-50 RT Grade) was used to separate the cathode and anode chambers. The entire H-cell was placed in a water bath in order to achieve adjustable temperatures. The CO_2R assessments were performed for at least 3 times after the water bath temperature was stabilized at the desired temperature for 10 min. During these CO_2R tests, the CO_2 gas flow rate was regulated by a mass flow controller (MFC, Alicat Scientific) at 25 mL min^{-1}.

CO_2/COR measurements in flow cell

All GDEs used in the CO_2/COR measurements in flow cell underwent treatment with a PTFE solution to enhance their hydrophobicity. The detailed procedure of this functionalization is as follows: 20 mL of ultrasonically treated 10 wt% PTFE solution was air-brushed evenly onto the gas diffusion layer of commercial GDE carbon paper (YLS-30T, 10 cm^2). Subsequently, the spray-coated carbon paper was transferred to a muffle furnace and calcined at 330 °C for 30 min under Ar. After the calcination procedure, the resulted GDE was then used for catalyst loading. It's important to note that our method can effectively address the variances in hydrophobicity between different batches of carbon paper, even from the same manufacturers, thereby enhancing the stability and repeatability of our catalytic experiments.

The working electrode was prepared through a spray-coating process. Specifically, 10 mg Cu-based catalyst was dispersed in a 2 mL isopropyl alcohol solution, containing 50 µL Nafion, followed by thorough ultrasonication. Subsequently, the catalyst precursor inks were air-brushed onto the micro porous layer of the carbon paper (YLS-30T). The catalyst loadings on each GDE electrodes were controlled to be ~0.6 mg/cm^2 by weighing the carbon paper electrodes before and after the catalyst coating with thorough drying.

The CO_2/COR performance were assessed using a customized flow electrolytic reactor (Supplementary Fig. 12), with 1 cm^2 as the active working electrode area. A reference electrode (Ag/AgCl with double salt bridge) and a counter electrode (Ni foam) were employed in our tests. Anion exchange membrane (AEM), Sustainion X37-50 RT Grade, was used to separate the cathode and anode chambers and the electrolytes. Besides, the electrolyte was circulated by a peristaltic pump at a liquid flow rate of 25 mL min^{-1}. The gas flow rate of CO_2 and CO was regulated by an MFC at 25 mL min^{-1}. Regarding the acidic CO_2R reaction, 0.5 M K_2SO_4 (pH = 2) was used as the electrolyte, and a proton exchange membrane (Nafion 117) was used. The other testing conditions were kept the same.

CO_2/COR measurements in MEA cell

The working electrode preparation in the MEA tests is nearly identical to what used in the flow cell, with the exception that the catalyst loading was increased to ~1.2 mg cm^{-2}. The MEA (1 cm^2 working area, Shanghai leinuo Technology company) setup was illustrated as in Supplementary Fig. 40.

The MEA was fabricated through a hot-pressing procedure involving a cathodic GDE (1 × 1 cm^2), an AEM (Sustainion X37-50 RT Grade, 1.5 × 1.5 cm^2, thickness 50µm), and an anodic IrO_x/Ti mesh (1 × 1 cm^2). The hot-pressing was carried out at 70 °C with a pressure of ~ 5 MPa for a duration of 1.5 min. Note that the AEM membrane was activated in 1 M KOH solution for 24 h before use.

In the MEA testing, 0.1 M $KHCO_3$ and 1 M KOH were used as the electrolytes for CO_2R. As for COR, 2 M KOH were used the electrolyte.

The anolyte temperature was kept as 80 °C to facilitate the oxygen evolution reaction (OER). The electrolyte flow rate was regulated by a peristaltic pump at a rate of 50 mL min^{-1}. The gas flow rate of CO_2/CO was controlled by an MFC at 25 mL min^{-1}.

Faradic efficiency

The Faradic Efficiency (FE) of each product in CO_2R or COR were estimated using the equation below:

$$FE(\%) = \frac{\text{amount of the product(mol)} \times n \times F}{C} \times 100 \quad (4)$$

where n is the number of electrons needed for a specific product, F is the Faradaic constant (96,485 C mol^{-1}). The amount of products (mol) were quantified by GC and NMR accordingly. C denotes for the total charge passing through during the catalysis.

Cathodic energy efficiency of C_{2+} products ($EE_{1/2}$)

For a specific C_{2+} product in $CO_{(2)}R$, such as ethylene, ethanol, acetate, and *n*-propanol, the half-cell energy efficiency of this product was estimated by the equation below:

$$EE_{\frac{1}{2}} = \frac{E^0_{CO2/product} - E^0_{OER}}{E^{applied}_{CO(2)R} - E^0_{OER}} \times FE \times 100\% \quad (5)$$

Where the $E^0_{CO2/product}$ and E^0_{OER} are the thermodynatic potentials for CO_2R to a specific product (cathodic reaction) and OER (anodic reaction), respectivley. FE is the faradic efficiency for the product measured at a given potentials. The thermodynatic potential for OER is 1.23 V vs. RHE. The themrodynamic potentials for different CO_2R products are listed in Supplementary Table 7. And the $EE_{1/2}$ of C_{2+} products is the sum of all individal proudcts.

Full cell energy efficiency of C_{2+} products

The full-cell energy efficiency for $CO_{(2)}R$ products was calculated by follow equation:

$$EE = \frac{(1.23 + (-E^0_A))}{-E^{Applied}_{cell\ voltage}} \times FE_{product} \times 100\% \quad (6)$$

Where E^0_A is the thermodynatic potential of $CO_{(2)}$ to the specific product[10]. $E^0_{Ethylene} = 0.17$ V_{RHE}; $E^0_{Ethanol} = 0.178$ V_{RHE}; $E^0_{acetate} = 0.454$ V_{RHE}; $E^0_{n-PrOH} = 0.2$ V_{RHE}. FE is the faradic efficiency for A at different potentials. $E^{Applied}_{cell\ voltage}$ is the measured cell voltage in the MEA system without any *iR* compensations.

Single-pass carbon efficiency (SPCE)

The SPCE for CO_2R was estimated based on the following equation:

$$SPCE = \frac{60s \times \sum\left(I \times x_i \times FE_{product} \div (n \times F)\right)}{\text{gasflowrate}\left(\frac{1}{min}\right) \times 1\,min \div 24.5\left(\frac{1}{mol}\right)} \quad (7)$$

Where I is the partial current density, FE_A is the FE of A, x_i is mole ratio of CO_2 to products ($x_i = 1$ for C1 products, $x_i = 2$ for C_2 products), n is the number of electrons needed for a specific produce, F is the Faradaic constant.

DFT calculations

All the calculations were performed with VASP at the spin-polarized GGA level with the Perdew–Burke–Ernzerhof exchange–correlation functional, and the projector-augmented-wave pseudopotential[74,75,76]. An energy cutoff of 400 eV was applied for the plan-wave basis set[75]. Cu(100) surface was selected because it has been proposed to be responsible for the C-C coupling[77]. The surface was described by a three-layer slab model with a vacuum layer of 14 Å. A 4 × 4 supercell was used with the Brillouin zone sampled by a 3 × 3 grid of Monkhorst-Pack k-points[78]. For the surface with 1/6 monolayer (ML) of Ga, a 3 × 4 supercell was used with a 4 × 3 grid of Monkhorst-Pack k-points. The dispersive interaction was treated with the DFT + D3 scheme[79]. Solvation effects were included with the implicit solvation model within VASPsol[80]. With the atoms in the bottom layer fixed to the bulk positions, the atoms in the up-two layers were allowed to relax until the maximum force on the atoms was smaller than 0.02 eV/Å. To simulate the CO-CO coupling process, two water molecules were adsorbed on the surface to stabilize the OCCO intermediates. Transition states were searched with the nudged elastic band method with climbing images[81]. The free energy profiles were calculated with the computational hydrogen electrode model[82]. Free energy corrections (including the zero-point energy, enthalpy, and entropy contributions) were included in the harmonic approximation[59]. The gas-phase molecules were treated as ideal gases. Energy corrections of 0.13 eV and −0.29 eV was applied to the CO_2 and CO molecules such that the calculated gas-phase thermochemical reaction enthalpies are consistent with the experimental values[83].

Data availability

Source data of this paper are provided in this paper and are also available from the corresponding authors upon request. Source data are provided with this paper.

References

1. Nitopi, S. et al. Progress and perspectives of electrochemical CO_2 reduction on copper in aqueous electrolyte. *Chem. Rev.* **119**, 7610–7672 (2019).
2. De Luna, P. et al. What would it take for renewably powered electrosynthesis to displace petrochemical processes? *Science* **364**, eaav3506 (2019).
3. Li, J. et al. Constraining CO coverage on copper promotes high-efficiency ethylene electroproduction. *Nat. Catal.* **2**, 1124–1131 (2019).
4. Dinh, C.-T. et al. CO_2 electroreduction to ethylene via hydroxide-mediated copper catalysis at an abrupt interface. *Science* **360**, 783–787 (2018).
5. Chen, L. et al. Additive-assisted electrodeposition of Cu on gas diffusion electrodes enables selective CO_2 reduction to multi-carbon products. *ACS Catal.* **13**, 11934–11944 (2023).
6. Wang, X. et al. Efficient electrically powered CO_2-to-ethanol via suppression of deoxygenation. *Nat. Energy* **5**, 478–486 (2020).
7. Wang, P. et al. Boosting electrocatalytic CO_2–to–ethanol production via asymmetric C–C coupling. *Nat. Commun.* **13**, 3754 (2022).
8. Ji, Y. et al. Selective CO-to-acetate electroreduction via intermediate adsorption tuning on ordered Cu–Pd sites. *Nat. Catal.* **5**, 251–258 (2022).
9. Luc, W. et al. Two-dimensional copper nanosheets for electrochemical reduction of carbon monoxide to acetate. *Nat. Catal.* **2**, 423–430 (2019).
10. Wang, X. et al. Efficient electrosynthesis of *n*-propanol from carbon monoxide using a Ag–Ru–Cu catalyst. *Nat. Energy* **7**, 170–176 (2022).
11. Niu, W. et al. Pb-rich Cu grain boundary sites for selective CO-to-n-propanol electroconversion. *Nat. Commun.* **14**, 4882 (2023).
12. Ozden, A. et al. Energy- and carbon-efficient CO_2/CO electrolysis to multicarbon products via asymmetric ion migration–adsorption. *Nat. Energy* **8**, 179–190 (2023).
13. Zhang, J. et al. Accelerating electrochemical CO_2 reduction to multi-carbon products via asymmetric intermediate binding at confined nanointerfaces. *Nat. Commun.* **14**, 1298 (2023).

14. Salvatore, D. & Berlinguette, C. P. Voltage matters when reducing CO_2 in an electrochemical flow cell. *ACS Energy Lett.* **5**, 215–220 (2020).
15. Fan, L. et al. Strategies in catalysts and electrolyzer design for electrochemical CO_2 reduction toward C2+ products. *Sci. Adv.* **6**, eaay3111 (2020).
16. Wang, Y., Han, P., Lv, X., Zhang, L. & Zheng, G. Defect and interface engineering for aqueous electrocatalytic CO_2 reduction. *Joule* **2**, 2551–2582 (2018).
17. Lee, S. Y. et al. Mixed copper states in anodized Cu electrocatalyst for stable and selective ethylene production from CO_2. *Reduct. J. Am. Chem. Soc.* **140**, 8681–8689 (2018).
18. De Luna, P. et al. Catalyst electro-redeposition controls morphology and oxidation state for selective carbon dioxide reduction. *Nat. Catal.* **1**, 103–110 (2018).
19. Huang, J., Mensi, M., Oveisi, E., Mantella, V. & Buonsanti, R. Structural sensitivities in bimetallic catalysts for electrochemical CO_2 reduction revealed by Ag–Cu nanodimers. *J. Am. Chem. Soc.* **141**, 2490–2499 (2019).
20. Feng, J. et al. Improving CO_2-to-C_{2+} product electroreduction efficiency via atomic lanthanide dopant-induced tensile-strained CuO_x catalysts. *J. Am. Chem. Soc.* **145**, 9857–9866 (2023).
21. Zheng, M. et al. Electrocatalytic CO_2-to-C_{2+} with ampere-level current on heteroatom-engineered copper via tuning *CO intermediate coverage. *J. Am. Chem. Soc.* **144**, 14936–14944 (2022).
22. Deng, B., Huang, M., Zhao, X., Mou, S. & Dong, F. Interfacial electrolyte effects on electrocatalytic CO_2 reduction. *ACS Catal.* **12**, 331–362 (2022).
23. Fang, M. et al. Hydrophobic, Ultrastable $Cu^{\delta+}$ for robust CO_2 electroreduction to C_2 products at ampere-current levels. *J. Am. Chem. Soc.* **145**, 11323–11332 (2023).
24. Ge, L. et al. Electrochemical CO_2 reduction in membrane-electrode assemblies. *Chem* **8**, 663–692 (2022).
25. Zhang, Z. et al. Membrane electrode assembly for electrocatalytic CO_2 reduction: principle and application. *Angew. Chem., Int. Ed. Engl.* **62**, e202302789 (2023).
26. Weng, L.-C., Bell, A. T. & Weber, A. Z. Towards membrane-electrode assembly systems for CO_2 reduction: a modeling study. *Energy Environ. Sci.* **12**, 1950–1968 (2019).
27. Lees, E. W. et al. Exploring CO_2 reduction and crossover in membrane electrode assemblies. *Nat. Chem. Eng.* **1**, 340–353 (2024).
28. Feng, J. et al. Modulating adsorbed hydrogen drives electrochemical CO_2-to-C2 products. *Nat. Commun.* **14**, 4615 (2023).
29. Liu, Z. et al. Interfacial water tuning by intermolecular spacing for stable CO_2 electroreduction to C_{2+} products. *Angew. Chem., Int. Ed. Engl.* **n/a**, e202309319 (2023).
30. Gileadi, E. *Physical Electrochemistry. Fundamentals, Techniques, and Applications*. (Wiley-VCH, 2011). ISBN: 978-3-527-31970-1.
31. Gileadi, E. *Physical Electrochemistry. Fundamentals, Techniques and Applications*. (Gulf Professional Publishing, 2021). ISBN:9780128243992.
32. Yang, H. et al. Carbon dioxide electroreduction on single-atom nickel decorated carbon membranes with industry compatible current densities. *Nat. Commun.* **11**, 593 (2020).
33. Hua, W. et al. A hierarchical Single-Atom Ni-N_3-C catalyst for electrochemical CO_2 reduction to CO with Near-Unity faradaic efficiency in a broad potential range. *Chem. Eng. J.* **446**, 137296 (2022).
34. Zhang, X. et al. Molecular engineering of dispersed nickel phthalocyanines on carbon nanotubes for selective CO_2 reduction. *Nat. Energy* **5**, 684–692 (2020).
35. Zheng, T. et al. Copper-catalysed exclusive CO_2 to pure formic acid conversion via single-atom alloying. *Nat. Nanotechnol.* **16**, 1386–1393 (2021).
36. Zhao, Y. et al. Spontaneously Sn-doped Bi/BiOx Core–Shell nanowires toward high-performance CO_2 electroreduction to liquid fuel. *Nano Lett.* **21**, 6907–6913 (2021).
37. Jia, B. et al. Indium cyanamide for industrial-grade CO_2 electroreduction to formic acid. *J. Am. Chem. Soc.* **145**, 14101–14111 (2023).
38. Joensen, B. Ó. et al. Unveiling transport mechanisms of cesium and water in operando Zero-Gap CO_2 electrolyzers. *Joule* **8**, 1–18 (2024).
39. Yang, K., Kas, R., Smith, W. A. & Burdyny, T. Role of the carbon-based gas diffusion layer on flooding in a gas diffusion electrode cell for electrochemical CO_2 reduction. *ACS Energy Lett.* **6**, 33–40 (2021).
40. Kim, B. et al. Trace-level cobalt dopants enhance CO_2 electroreduction and ethylene formation on copper. *ACS Energy Lett.* **8**, 3356–3364 (2023).
41. Clark, E. L., Hahn, C., Jaramillo, T. F. & Bell, A. T. Electrochemical CO_2 reduction over compressively strained CuAg surface alloys with enhanced multi-carbon oxygenate selectivity. *J. Am. Chem. Soc.* **139**, 15848–15857 (2017).
42. Wei, Z. et al. Enhancing selective electrochemical CO_2 reduction by in situ constructing tensile-strained Cu catalysts. *ACS Catal.* **13**, 4711–4718 (2023).
43. Hansen, H. A., Shi, C., Lausche, A. C., Peterson, A. A. & Nørskov, J. K. Bifunctional alloys for the electroreduction of CO_2 and CO. *Phys. Chem. Chem. Phys.* **18**, 9194–9201 (2016).
44. Guan, A. et al. Steric effect induces CO electroreduction to CH_4 on Cu–Au alloys. *J. Mater. Chem. A* **9**, 21779–21784 (2021).
45. Zhao, J. et al. Modulation of *CHxO adsorption to facilitate electrocatalytic reduction of CO_2 to CH_4 over Cu-Based Catalysts. *J. Am. Chem. Soc.* **145**, 6622–6627 (2023).
46. Castilla-Amorós, L., Chien, T.-C. C., Pankhurst, J. R. & Buonsanti, R. Modulating the reactivity of liquid Ga nanoparticle inks by modifying their surface chemistry. *J. Am. Chem. Soc.* **144**, 1993–2001 (2022).
47. Liu, H. et al. Solid–liquid phase transition induced electrocatalytic switching from hydrogen evolution to highly selective CO_2 reduction. *Nat. Catal.* **4**, 202–211 (2021).
48. Zhan, P. et al. Synthesis of AuX (X = Ni, Ga, Mo, Zn, and Cr) alloy aerogels as high-performance electrocatalytic CO_2 reduction reaction catalysts. *Langmuir* **39**, 8306–8313 (2023).
49. Tran, K. & Ulissi, Z. W. Active learning across intermetallics to guide discovery of electrocatalysts for CO_2 reduction and H2 evolution. *Nat. Catal.* **1**, 696–703 (2018).
50. Okatenko, V. et al. The native oxide skin of liquid metal ga nanoparticles prevents their rapid coalescence during electrocatalysis. *J. Am. Chem. Soc.* **144**, 10053–10063 (2022).
51. Okatenko, V. et al. Alloying as a strategy to boost the stability of copper nanocatalysts during the electrochemical CO_2 reduction reaction. *J. Am. Chem. Soc.* **145**, 5370–5383 (2023).
52. Li, P. et al. p–d Orbital hybridization induced by *p*-block metal-doped Cu promotes the formation of C_{2+} products in ampere-level CO_2 electroreduction. *J. Am. Chem. Soc.* **145**, 4675–4682 (2023).
53. Yan, S. et al. High-power CO_2-to-C_2 electroreduction on Ga-spaced, square-like Cu sites. *J. Am. Chem. Soc.* **145**, 26374–26382 (2023).
54. Ummireddi, A. K., Li, Z. & Wu, J. Copper defects for CO_2 electrocatalysis toward a specific multicarbon product. *Trends Chem.* **5**, 170–173 (2023).
55. Cheng, D. et al. The nature of active sites for carbon dioxide electroreduction over oxide-derived copper catalysts. *Nat. Commun.* **12**, 395 (2021).
56. Chen, Z. et al. Grain-boundary-rich copper for efficient solar-driven electrochemical CO_2 reduction to ethylene and ethanol. *J. Am. Chem. Soc.* **142**, 6878–6883 (2020).
57. Zong, Y., Chakthranont, P. & Suntivich, J. Temperature effect of CO_2 reduction electrocatalysis on copper: potential dependency of activation energy. *J. Electrochem. En. Conv. Stor* **17**, 041007 (2020).

58. Vos, R. E. et al. How temperature affects the selectivity of the electrochemical CO_2 reduction on copper. *ACS Catal.* **13**, 8080–8091 (2023).
59. Peterson, A. A., Abild-Pedersen, F., Studt, F., Rossmeisl, J. & Nørskov, J. K. How copper catalyzes the electroreduction of carbon dioxide into hydrocarbon fuels. *Energy Environ. Sci.* **3**, 1311–1315 (2010).
60. Wu, H. et al. Selective and energy-efficient electrosynthesis of ethylene from CO_2 by tuning the valence of Cu catalysts through aryl diazonium functionalization. *Nat. Energy* **9**, 422–433 (2024).
61. Arán-Ais, R. M., Scholten, F., Kunze, S., Rizo, R. & Roldan Cuenya, B. The role of in situ generated morphological motifs and Cu(I) species in C_{2+} product selectivity during CO_2 pulsed electroreduction. *Nat. Energy* **5**, 317–325 (2020).
62. Li, J. et al. Selective CO_2 electrolysis to CO using isolated antimony alloyed copper. *Nat. Commun.* **14**, 340 (2023).
63. Bratsch, S. G. Standard electrode potentials and temperature coefficients in water at 298.15 K. *J. Phys. Chem. Ref. Data* **18**, 1–21 (1989).
64. Gunathunge, C. M. et al. Spectroscopic observation of reversible surface reconstruction of copper electrodes under CO_2 reduction. *J. Phys. Chem. C.* **121**, 12337–12344 (2017).
65. Yang, X. et al. Mechanistic insights into C-C coupling in electrochemical CO reduction using gold superlattices. *Nat. Commun.* **15**, 720 (2024).
66. Hou, J. et al. Influence of electric double layer rigidity on CO adsorption and electroreduction rate. *Nat. Commun.* **15**, 1926 (2024).
67. Ma, W. et al. Copper lattice tension boosts full-cell CO electrolysis to multi-carbon olefins and oxygenates. *Chem* **9**, 2161–2177 (2023).
68. Cheng, T., Xiao, H. & Goddard, W. A. Full atomistic reaction mechanism with kinetics for CO reduction on Cu(100) from ab initio molecular dynamics free-energy calculations at 298 K. *Proc. Natl Acad. Sci. USA* **114**, 1795–1800 (2017).
69. Eilert, A. et al. Subsurface oxygen in oxide-derived copper electrocatalysts for carbon dioxide reduction. *J. Phys. Chem. Lett.* **8**, 285–290 (2017).
70. Kim, J. Y. T., Sellers, C., Hao, S., Senftle, T. P. & Wang, H. Different distributions of multi-carbon products in CO_2 and CO electroreduction under practical reaction conditions. *Nat. Catal.* **6**, 1115–1124 (2023).
71. Zhang, T. et al. The conventional gas diffusion electrode may not be resistant to flooding during CO_2/CO Reduction. *J. Electrochem. Soc.* **169**, 104506 (2022).
72. Popović, S. et al. Stability and degradation mechanisms of copper-based catalysts for electrochemical CO_2 Reduction. *Angew. Chem., Int. Ed. Engl.* **59**, 14736–14746 (2020).
73. Vavra, J., Shen, T.-H., Stoian, D., Tileli, V. & Buonsanti, R. Real-time monitoring reveals dissolution/redeposition mechanism in copper nanocatalysts during the initial stages of the CO_2 reduction reaction. *Angew. Chem., Int. Ed. Engl.* **60**, 1347–1354 (2021).
74. Kresse, G. & Furthmüller, J. Efficient iterative schemes for ab initio total-energy calculations using a plane-wave basis set. *Phys. Rev. B* **54**, 11169–11186 (1996).
75. Blöchl, P. E. Projector augmented-wave method. *Phys. Rev. B* **50**, 17953–17979 (1994).
76. Kresse, G. & Furthmüller, J. Efficiency of ab-initio total energy calculations for metals and semiconductors using a plane-wave basis set. *Comput. Mater. Sci.* **6**, 15–50 (1996).
77. Schouten, K. J. P., Qin, Z., Pérez Gallent, E. & Koper, M. T. M. Two pathways for the formation of ethylene in CO reduction on single-crystal copper electrodes. *J. Am. Chem. Soc.* **134**, 9864–9867 (2012).
78. Monkhorst, H. J. & Pack, J. D. Special Points for Brillouin-Zone Integrations. *Phys. Rev. B* **13**, 5188–5192 (1976).
79. Grimme, S., Ehrlich, S. & Goerigk, L. Effect of the Damping Function in Dispersion Corrected Density Functional Theory. *J. Comput. Chem.* **32**, 1456–1465 (2011).
80. Mathew, K., Sundararaman, R., Letchworth-Weaver, K., Arias, T. A. & Hennig, R. G. Implicit solvation model for density-functional study of nanocrystal surfaces and reaction pathways. *J. Chem. Phys.* **140**, 084106 (2014).
81. Henkelman, G., Uberuaga, B. P. & Jónsson, H. A climbing image nudged elastic band method for finding saddle points and minimum energy paths. *J. Chem. Phys.* **113**, 9901–9904 (2000).
82. Nørskov, J. K. et al. Origin of the overpotential for oxygen reduction at a fuel-cell cathode. *J. Phys. Chem. B* **108**, 17886–17892 (2004).
83. Han, N. et al. Ultrathin bismuth nanosheets from in situ topotactic transformation for selective electrocatalytic CO_2 reduction to formate. *Nat. Commun.* **9**, 1320 (2018).

Acknowledgements

We acknowledge the National University of Singapore and Ministry of Education for their financial support, through the grants A-0009176-02-00 and A-0009176-03-00, as well as A*STAR (Agency for Science, Technology and Research) under its LCERFI program (award no. U2102d2002). We would also like to acknowledge the support of the National Research Foundation (NRF) Singapore, under the NRF Fellowship (NRF-NRFF13-2021-0007) and CRP (NRF-CRP27-2021-0004), as well as the support from the Center for Hydrogen Innovations at the NUS (CHI-P2022-06; A-8000138-03-00). Y.J. also would like to acknowledge the Natural Science Foundation of Guangdong Province (2023A1515012238), and Guangzhou Municipal Science and Technology Bureau (202201020145).

Author contributions

L.W. and L.C. conceived and designed this project. Y.J. conducted the computational calculation and relative data analysis. L.C., J.C., W.F., and D.W. synthesized the catalysts and conducted the electrochemical experiments. L.C. and Y.X. carried out the ex-situ physical characterizations. L.C. and J.C. conducted the operando XAS experiments under the supervision of S.X. Everyone contributed to data analysis, writing, and editing of the manuscript. L.W. supervised the entire project.

Competing interests

The authors declare no competing interests.

Additional information

Supplementary information The online version contains supplementary material available at https://doi.org/10.1038/s41467-024-51466-8.

Correspondence and requests for materials should be addressed to Yongfei Ji or Lei Wang.

Peer review information *Nature Communications* thanks Xuan Yang, Siddhartha Subramanian, and the other, anonymous, reviewer(s) for their contribution to the peer review of this work. A peer review file is available.